Acta Materialia 311 (2026) 122216

Contents lists available at ScienceDirect

Acta Materialia

journal homepage: www.elsevier.com/locate/actamat

Full length article

Integrating artificial intelligence with experimental and computational materials science to predict crystallization in multicomponent glasses

Marco Bertani [a], Matilde Benassi [a], Lorenzo Gottardi [a], Gianluca Malavasi [a], Ashutosh Goel [b,*], Alfonso Pedone [a,*]

[a] Department of Chemical and Geological Sciences, University of Modena and Reggio Emilia, Via Campi, 103, 41125 Modena, Italy
[b] Department of Materials Science and Engineering, Rutgers, The State University of New Jersey, Piscataway, NJ 08854, USA

ARTICLE INFO

Keywords:
Molecular dynamics simulations
Oxide glasses
Crystallization
Machine learning

ABSTRACT

Crystallization profoundly influences the performance of glasses, governing their stability in nuclear waste forms, manufacturability in industrial systems, and functionality in glass-ceramics. However, the predictive models remain elusive due to the structural complexity of multicomponent glasses. Here, we establish a data-driven framework that integrates systematic experimental datasets, atomistic simulations and machine learning to predict crystallization in multicomponent alkali aluminoborosilicate glasses designed in the primary crystallization field of nepheline ($NaAlSiO_4$). Molecular dynamics models, validated against multinuclear MAS NMR spectra, reveal medium-range order and cluster motifs that are structurally similar to nepheline. From this, we derived a structural descriptor—the mean cumulative displacement (MCD)—that quantifies structural similarity between the glass and nepheline crystal. When combined with optical basicity, MCD enables robust separation of crystallizing and non-crystallizing glasses. A support vector machine (SVM) classifier trained on MCD and OB achieved $\geq$94% accuracy across 88 glass compositions, yielding interpretable decision boundaries that link chemistry, structure, and crystallization behavior. While the present study focuses on nepheline crystallization, the methodology provides a structure-based framework that could be extended to other crystalline phases and glass families in future work.

1. Introduction

Crystallization is a fundamental phenomenon that bridges the worlds of order and disorder, governing transformations that are critical across science, engineering, and technology. From the controlled solidification of metals and semiconductors to the stability of pharmaceuticals and the durability of glasses, the onset of crystallization dictates both performance and reliability. Nowhere is this more evident than in amorphous materials, where the lack of long-range order offers both remarkable opportunities and unique challenges. Glasses, for example, are indispensable in fields as diverse as photonics, electronics, structural applications, medicine, and energy, yet their utility often hinges on whether crystallization can be harnessed or suppressed [1–6]. Crystallization can either enhance functionality—as in glass-ceramics where mechanical strength or thermal stability is improved through controlled devitrification—or lead to detrimental effects, such as the premature degradation of glasses intended for long-term containment or high-performance applications [7].

Despite its technological importance, crystallization in amorphous materials remains poorly understood at a predictive level. The central difficulty lies in the disordered nature of the glassy state: lacking periodicity, glasses exhibit a rich diversity of local environments that complicates the identification of universal principles governing nucleation and growth. Classical models have provided useful guidelines, correlating composition with crystallization tendencies through simplified descriptors or empirical rules [7–9]. However, such approaches rarely generalize across the vast landscape of multicomponent glasses, limiting their power to guide the rational design of new materials [10]. Emerging research increasingly points to the need for models that bridge chemistry, structure, and dynamics at the atomic scale—linking short- and medium-range order to macroscopic crystallization behavior. Meeting this challenge is not only a scientific imperative but also a technological necessity for advancing the next generation of glass-based systems.

In this context, nepheline ($NaAlSiO_4$) crystallization serves as a

* Corresponding authors.
E-mail addresses: ag1179@soe.rutgers.edu (A. Goel), alfonso.pedone@unimore.it (A. Pedone).

https://doi.org/10.1016/j.actamat.2026.122216
Received 3 October 2025; Received in revised form 27 February 2026; Accepted 6 April 2026
Available online 7 April 2026

series) led to a transition from metaluminous to peralkaline glass, while P_2O_5 substitution for SiO_2 (SPB-*y*) or B_2O_3 (BP-*z*) maintained the metaluminous nature. The values of x and y varied from 0 to 15 mol.%, whereas z varied up to 10 mol.%. Among these glasses, nepheline/low-carnegieite crystallized in AP-*x* and SPB-*y* glasses with x and $y \leq 5$ mol.%, and all the glasses of the BP-*z* series.

6 ***xFeyP* series** (extracted from ref [28]): This glass series was designed to investigate the impact of Fe_2O_3 and P_2O_5 on the structure and crystallization behavior of sodium aluminoborosilicate glasses. The glasses have compositions (100-*y*) [25 Na_2O – (15-*x*) Al_2O_3 – x Fe_2O_3 – 15 B_2O_3 – 45 SiO_2] with x varying between 0 and 5 mol.%, and y between 0 and 7.5 mol.%. The batched compositions are reported in **Table S6**. The addition of Fe_2O_3 tends to lower the nepheline crystallization, but it does not suppress it. P_2O_5 suppresses nepheline crystallization both in Fe-free and Fe-containing compositions. Experimental data reported in the article indicate that the addition of P_2O_5 promotes the formation of Fe^{2+}, leading to the depolymerization of glass network. The $Fe^{3+}/\sum Fe$ in the simulated glasses were in accordance with the values reported in the original study based on Mossbauer spectroscopy [28]. A semi-quantitative crystalline-to-amorphous phase analysis of the X-ray diffraction data was carried out using the Rietveld–reference intensity ratio (RIR) method, with 10 wt.% Al_2O_3 (NIST SRM 676A) as the internal standard. The experimental results pertaining to the crystallization behavior of glasses were in agreement with the predictions of the optical basicity model.

7 **LK-*x* and HK-*x* series**: These glass series was designed to investigate the impact of K_2O on the crystallization of nepheline. The experimental data is unpublished yet, but it has been produced following the experimental protocols similar to those reported for CaB-*x* and NCB-*x* glasses [29]. The LK-*x* series was designed to have OB values lower than 0.57 and has a composition (20-*x*) Na_2O – x K_2O – 15 Al_2O_3 – 20 B_2O_3 – 45 SiO_2 with x varying from 0 to 20 mol.%, where $\Delta x = 5$ mol.%, while the HK-*x* series was designed to have OB higher than 0.57 and has compositions (24-*x*) Na_2O – x K_2O – 16 Al_2O_3 – 16 B_2O_3 – 44 SiO_2 with x varying from 0 to 24 mol.%, where $\Delta x = 6$ mol.%. The batched compositions are reported in **Table S7**. Consistent with predictions from the OB model [10] experimental results show that all glasses in the HK-*x* series crystallize nepheline ($NaAlSiO_4$), its K-containing analogue kalsilite ($KalSiO_4$), or their solid solution $Na_{(1-x)}K_xAlSiO_4$. The concentration of crystalline phase in the samples varies between 1 – 15 wt.% and tends to increase with increasing the OB of glass. Because nepheline and kalsilite are known to form a complete solid solution across the Na–K aluminosilicate system [30], this possibility has been explicitly considered in the present study. In contrast, glasses in the LK-*x* series with OB < 0.57 remain fully amorphous after CCC treatment.

8 **SP-*x* Glass Series** (extracted from ref [31]): The glasses in the system 25 Na_2O – 25 Al_2O_3 –x P_2O_5 – (50-*x*) SiO_2, where x varies between 0 – 35 mol.%; $\Delta x = 5$ mol.%, were investigated to understand the impact of P_2O_5 on their crystallization behavior. **Table S8** presents the experimental compositions of the investigated glasses, as analyzed by wavelength dispersive X-ray fluorescence (WD-XRF) spectroscopy in ref [31]. The experimental results pertaining to the crystallization behavior of glasses reveal that substituting ~10 mol.% SiO_2 with P_2O_5 suppresses the crystallization in glasses. Based on the analysis of ^{29}Si, ^{27}Al, ^{31}P MAS NMR spectroscopy, the authors attributed the suppression of crystallization to the formation of Al–O–P linkages, thus resulting in a decrease in the concentration of Si–O–Al bonds, crucial for nepheline crystallization. Here it should be noted that the heat-treatment schedule employed to study the crystallization behavior of the SP-*x* glass series in ref [20] was different with respect to that used in the other investigations [24,25]: specifically, a dwell time of 30 min (instead of 24 h) was applied in the crystallization region. Due to this reason, the authors re-synthesized and characterized these glasses, as described in Section 2 of the supplementary information document. **Figs. S1** and **S2** show the DTA and the XRD patterns whereas **Tables S9-S11** the glass compositions, glass and crystallization temperatures and crystallization behavior. The new results reveal that with a dwelling time of 24 h nepheline is the primary crystallization phase up to SP-15 glass and a secondary phase in the SP-25 glass. Beyond SP-20, however, $AlPO_4$ becomes the main crystalline phase.

4. Computational methodology

4.1. MD simulations

Structural models for the investigated glasses, as mentioned earlier, were generated using classical MD simulations. Each composition was modeled in simulation boxes containing approximately 10,000 atoms for structural and cluster analysis and 400 atoms for MAS NMR simulation. The precise number of atoms and the corresponding box dimensions are provided in **Tables S12** and **S13.**

The force field used in these simulations is based on the shell model [32] in which oxygen atoms are represented by a massive, positively charged core and a massless, negatively charged shell, connected via a harmonic spring. The combined charges of the core and shell yield the formal charge of oxygen atoms (−2e). Beyond the harmonic interaction with their respective cores, the oxygen shells interact with each other and with the surrounding cations through short-range Buckingham potentials, while electrostatic interactions occur among all species carrying full formal charges. Additionally, three-body screened harmonic potentials are employed to regulate the O–T–O (T = Si, Al, P, Fe) angles within tetrahedra. The complete functional form of the potential is given in Eq. (1):

$$U(r_{ij}, r_{c-s}, \theta_{ijk}) = \frac{z_i z_j e^2}{r_{ij}^2} + A_{ij} e^{-\left(\frac{r_{ij}}{\rho_{ij}}\right)} - \frac{C_{ij}}{r_{ij}^6} + \frac{1}{2} k_s (r_c - r_S)^2 + \frac{1}{2} k_b \left(\theta_{ijk} - \theta_{ijk}^0\right)^2 e^{-\left(\frac{r_{ij}}{\rho} + \frac{r_{jk}}{\rho}\right)} \quad (1)$$

This force field has been already demonstrated to reliably reproduce the medium-range structure of oxide glasses and especially the Si speciation and inter-tetrahedra bond angle distributions [17,33–36].

All the parameters used in this work are reported in **Table S14**. It needs to be emphasized that for the B–O interaction, two sets of parameters were used: the first developed by Stevensson et al. [37] and second refined by Pedone et al. [38]. The second set is a modification of the first set of parameters, more suitable for compositions presenting high N_4 ($= \frac{BO_4}{BO_3 + BO_4}$) fractions. For this reason, glasses presenting $N_4 > 0.25$ were simulated with the Pedone's potential to improve the structural accuracy and are highlighted in the tables reporting the compositions.

The leapfrog algorithm, as implemented in the DL_POLY2.14 package, [39] was used to integrate the equations of motion with a 0.2 fs timestep. Initial configurations were generated by randomly placing atoms in cubic boxes sized to match the experimental densities. Systems were heated to 3200 K for 50 ps under the NVT ensemble, using the Berendsen thermostat [40] with a friction coefficient of 0.2 ps to ensure complete melting. The liquids were then quenched to 300 K at a nominal rate of 5 K/ps and equilibrated for 100 ps. Velocity scaling was applied at each step to control the kinetic energy of the shells. Coulomb interactions were computed using the Ewald summation method [41] with an 8 Å cutoff, while a 7.5 Å cutoff was used for short-range van der Waals interactions.

4.2. Simulations of MAS NMR spectra

The ^{27}Al, ^{11}B, ^{23}Na, ^{31}P, and ^{29}Si MAS NMR spectra of the representative glasses have been simulated by adopting the MD-GIPAW approach [42–44] coupled with Solid State NMR (SoSNMR) code [45] used in our previous work [46–52]. The computational details are reported in the supplementary information.

4.3. Cluster analysis and mean cumulative displacement (MCD) descriptor

The model used in this work assumes that structural similarity between local atomic environments in the glass and the corresponding crystalline phase correlates with the experimentally observed tendency toward crystallization. In this context, clusters of atoms ('embryos') refer to glass regions exhibiting local structural similarity to the crystal, without implying direct observation of nucleation events or growth mechanisms. The cluster analysis explores simulated structures, quantifying the similarity between the atomic environments in glass and the reference crystal. Atomic aggregates (clusters) within a pre-defined cutoff from the central atom in the glass model are compared with those of a reference crystalline structure, providing a cumulative displacement between the radial distribution function up to the predefined cutoff. An in-depth description of the cluster analysis and its algorithm has been reported elsewhere [18].

In the present investigation, we focused on the local environment of oxygen atoms within a cutoff of 7 Å (the optimization of this value is detailed in **Fig. S3** of the ESI), which can be compared with six different oxygen sites in the nepheline crystal. The algorithm seeks for the best oxygen-centered clusters in the glass with the minimum cumulative displacement with respect to the six oxygen sites in the nepheline crystals and then computes the Mean Cumulative Displacement (MCD) by averaging them.

Initially, the cluster analysis calculated the MCD using the basic common form of nepheline, which includes only Na, Al, Si, and O atoms. At a later stage, we extended the code to account for the substitution of Fe^{3+} for Al^{3+} and K^+ for Na^+ in the nepheline crystal structure. As for the Fe^{3+}/Al^{3+} substitution, we used a replacement threshold that varies according to the Fe_2O_3 concentration in the glass: the equation describing this dependency is fitted to experimental data present in ref [53] and is illustrated in **Fig. S4** of the ESI. Instead, for the $K^+ \leftrightarrow Na^+$ substitution we allowed it in the entire compositional range (up to 100%).

An alternative descriptor derived from cluster analysis is the fraction of oxygen atoms in the glass whose cumulative displacement falls below a user-defined threshold, denoted as $D_{threshold}$ (e.g., D_{80}, D_{90}, D_{100}). This metric not only indicates the presence of embryonic structures in the glass but also enables their quantification. Based on the test shown in **Fig. S5** of the ESI, the D_{100} descriptor was selected, consistent with the threshold previously adopted for MCD-based classification in our earlier work [21]. Subsequently, Principal Component Analysis (PCA) was performed on these and other structural and compositional parameters, for example, optical basicity, fraction of Al/Fe–O–Si bridges, amount of Na^+/K^+ coordinated by oxygen involved in Al/Fe–O–Si bonds, Si–Na^+/K^+ and Al–Na^+/K^+ coordination numbers, oxygen speciation. The goal was to identify the most influential parameters to be used in ML classifier algorithm for predicting nepheline crystallization.

4.4. Machine learning classifiers (MLC)

To develop an analytical classification model capable of predicting the propensity of a glass to precipitate nepheline, we evaluated the performance of eight different MLCs. In particular, we tested the K-Nearest Neighbor (KNN, using 5 neighbors), Random Forest (RF), Gradient Boosting (GB), and Support Vector Machine (SVM) algorithms. For the SVM algorithm, linear, polynomial (degree = 2, 3, and 4), and gaussian (RBF) kernels were employed.

Model training and performance assessment were performed using a 5-fold repeated cross-validation (CV) strategy. The dataset, comprising 88 glasses, was randomly partitioned into five subsets (three containing 17 compositions and two containing 18), ensuring that each composition was used once for testing and four times for training in each CV repetition. This procedure was repeated five times with different random partitions, using a fixed seed to reduce the dependence on a specific train–test split and to assess the robustness of the classification outcomes. The distribution of crystallizing and non-crystallizing compositions across the folds of the repeated 5-fold CV procedure is shown in **Fig. S6**, indicating that none of the folds contains only glasses from a single class.

The BL_Li glass, which behaves as an outlier in the descriptor space and whose anomalous position cannot currently be unambiguously rationalized, was excluded from the training sets and treated as an external test case. Including this composition in the training folds was found to introduce large fluctuations in the learned decision boundaries due to the limited dataset size. BL_Li was therefore used solely to probe the extrapolative robustness of the trained models and was not included in the cross-validation statistics.

To confirm the absence of overfitting and to assess the convergence of predictive performance with respect to dataset size, we generated learning curves for all classifiers by progressively increasing the number of training samples from 20 up to the full set of 88 compositions. At each size, subsets were randomly selected while preserving the crystallizing/non-crystallizing ratio, and the same repeated 5-fold cross-validation protocol used in the final models was applied. The results, reported in **Fig. S7** of the ESI, show that validation accuracy steadily increases and plateaus after approximately 65 samples. The gap between training and validation accuracy remains essentially constant across all dataset sizes and is mainly associated with the presence of BL_Li compositions in the test folds.

All algorithms were implemented in a custom Python script utilizing the *scikit-learn* and *seaborn libraries*.

5. Results and discussion

5.1. Validation of MD-derived structural models

As noted, in Section 2, establishing the reliability of MD simulations is essential for any predictive model linking MD-derived glass structures to crystallization behavior. To validate our simulations, we compared simulated MAS NMR spectra of key spin-active nuclei, generated using the MD-GIPAW approach, with their respective experimental spectra. Since it was impractical to simulate spectra for all the investigated glasses, we selected representative samples from each series.

These glasses were chosen based on the availability of reliable experimental MAS NMR spectra reported in previous studies and their representativeness of the typical coordination environments and network connectivity within each series.

Specifically, we simulated the ^{27}Al MAS NMR spectrum for Alum-3, BL-neph, CaB-10, BL-P, SP-10, and AP-15 glasses; ^{11}B MAS NMR spectrum for Alum-3, CaB-10, BL-P, and AP-15 glasses; ^{29}Si MAS NMR spectra for BL-neph, BL-P, and AP-15 glasses; ^{23}Na MAS NMR spectrum for BL-neph; and ^{31}P MAS NMR spectrum for SP-10 and AP-15. These spectra, along with experimental conditions, are reported in **Figs. S8-S11**.

In **Fig. S8**, the experimental and simulated ^{27}Al MAS NMR spectra of Alum-3 (panel a), BL-neph (panel b), CaB-10 (panel c), BL-P (panel d), AP-15 (panel e), and SP-10 (panel f) glasses are reported. The simulated spectra (red line) for all glasses align within the expected 40−60 ppm chemical shift range for four-fold-coordinated Al. However, they exhibit asymmetrical broadening compared to experimental spectra (black line) collected at lower fields (11 T –16.4 T), where quadrupolar broadening is not fully eliminated. In contrast, the simulated ^{27}Al MAS spectrum for BL-neph (collected at 21 T) shows close agreement with the experimental data, accurately capturing both the chemical shifts and the local environment of Al. Previous studies [35,54] suggest that our models tend to overestimate quadrupolar coupling constants (C_Q) due to increased disorder and structural overestimation of Al–O–Al bonds and three-bridging oxygens (TBOs). A C_Q correction of 0.6 achieves near-perfect alignment between simulated (blue lines) and experimental data. It is worth to highlight that this correction does not alter the underlying atomic structure used for the extraction of the MCD and other structural descriptors. Instead, it is applied only at the level of NMR spectral reconstruction to account for known limitations in reproducing absolute quadrupolar coupling. Indeed, the spectra acquired at very high magnetic fields (see spectra of BL-neph glass in panel (b) of Fig. S9) where the spectrum is primarily governed by the distribution of isotropic chemical shifts (negligible second-order quadrupolar effects) are very well reproduced by our simulations. Experimental NMR confirms that Al is consistently four-fold coordinated across these glasses, a result our models also replicate, indicating reliable Al environments despite the quenching rates used.

Fig. S9 indicates that the ^{29}Si MAS NMR spectra for BL-neph (panel a), AP-15 (panel b), and BL-P (panel c) glasses are also well represented, featuring a single broad peak between −80 and −100 ppm. Our MD models capture the qualitative distribution of Q^n (*m* Al, B) species, where *Q* denotes quaternary species with *n* bridging oxygens linked to Si, and *m* represents the number of AlO_4 and BO_3 or BO_4 units attached to SiO_4 unit, suggesting a good structural alignment with experimental observations.

Fig. S10 presents the ^{31}P MAS NMR spectra of AP-15 (panel a) and SP-10 (panel b) glasses, and the ^{23}Na MAS NMR spectrum of BL-neph (panel c). The latter is well reproduced, indicating that our models accurately capture Na environments. The experimental ^{31}P MAS NMR spectrum of AP-15 (black line) shows a single peak at −8 ppm, while SP-10 exhibits a peak at −10 ppm with a shoulder near 0 and 22 ppm.

Peak assignments in P_2O_5-containing alkali/alkaline-earth silicate glasses depend on the presence of B_2O_3 and/or Al_2O_3. Typically, two peaks are observed: (1) 0–16 ppm for P^0 [$(PO_4)^{3-}$] units, and (2) ∼ −5 ppm for P^1 [$(P_2O_7)^{4-}$] units [55] The P^n nomenclature denotes the number of bridging oxygens per phosphorus atom.

In glasses with B_2O_3, e.g., 25 Na_2O – 20 B_2O_3 – *x* P_2O_5 – (55-*x*) SiO_2 (mol.%), three peaks emerge in the ^{31}P MAS NMR spectra: ∼16 ppm (P^0), 1–4 ppm (P^1), and −5 to −10 ppm corresponding to mix of P^2_{2B} and $P^2_{1B,\,1P}$ units [56] In Na_2O – Al_2O_3 (– B_2O_3) – P_2O_5 – SiO_2 systems, assignments are less clear due to overlapping peaks from diverse phosphate species (e.g., $P^0{}_{xAl,B}$, $P^1{}_{xAl,B}$, $P^2{}_{xAl,B}$) [31,57–59] reflecting compositional complexity and structural diversity, which is difficult to capture on the sole basis of chemical shift of ^{31}P MAS NMR spectrum.

In the present study, we have adopted the peak assignments from our prior work, identifying six features: (1) ∼16.5 ppm (P^0), (2) ∼7.5 ppm (P^1_{1T}, T = AlO_4 or BO_4), (3) ∼3.5 ppm (P^1), (4) ∼ −1.8 ppm P^2_{2T}, i.e., P^2 unit connected with 2 AlO_4 or 2 BO_4 units or 1 AlO_4 and 1 BO_4 units, (5) −9 ppm (P^2_{1T}), and (6) −16 ppm (P^2). The simulated spectrum (red line), however, shows a distinctly different shape, with each species contributing as separate peaks. In the ^{31}P MAS NMR spectra of glass AP-15, the small peak at 15 ppm corresponds to P^0 units, while the peak at −8 ppm corresponds to P–O–B linkages in P^2 units and is well aligned with the experimental spectra, while the shoulder at −14 ppm is associated with P^2 species. Additionally, the shoulder at −25 ppm and the small peak at −40 ppm are attributed to P^3 and P^4 species, which are absent in the experimental structure [26]. The experimentally acquired ^{31}P MAS NMR spectra of glass SP-10 is dominated by the peak at −10 ppm, associated with P^3 species with three P–O–Al bonds, and by two smaller shoulders around 0 ppm and 22 ppm given by P^2 and P^4 species with P-O-Al bonds, respectively. The simulated glasses show a good agreement with the P^n speciation (see **Table S15**), but the spectra are broader with signals given by the contribution of P–O–Si bonds, not reported experimentally, which corresponds to almost 20% of the bonds involving P. This suggest that more accurate interatomic potentials should be developed to improve phosphorous second coordination spheres in silicophosphate glasses.

Fig. S11 compares the simulated (red line) and experimental ^{11}B MAS NMR spectra for Alum-3 (a), CaB-10 (b), BL-P (c), and AP-15 (d) glasses. While the simulations broadly capture the experimental features, the peaks appear noticeably broader, indicating a more disordered boron environment in the modeled structures. Both experimental and simulated ^{11}B MAS NMR spectra exhibit two characteristic peaks: one between 10 and 20 ppm corresponding to BO_3 units, and another near 0 ppm attributed to BO_4 units. The AP-15 glass spectrum was simulated using Pedone's B–O interaction parameters [60], yielding a good estimate of the BO_3/BO_4 ratio and a well-matched peak shape, albeit with a slight underestimation of the BO_4 peak position. Following what was stated for the ^{27}Al MAS NMR spectra, we corrected the C_Q interaction with a factor of 0.8 to balance its overestimation given by the increased disorder. The corrected spectra are presented in blue color in **Fig. S11** and show better agreement with experimental ^{11}B MAS NMR spectra of all the glasses.

Fig. S12 provides a correlation plot of computed and experimental BO_4 species across the glass series, showing general agreement (mean absolute error of 4.44%), with a few outliers where BO_4 is underestimated (BO_3 is overestimated). This figure also shows a comparison of the %BO_4 for some compositions obtained with Stevensson's [61]and Pedone's B–O parameters to prove that the latter give better agreement at high N_4 fractions.

The glass structures studied are generally well captured using the core-shell potential, with only minor discrepancies in the medium-range environment of the phosphate component. This validates the model's reliability for constructing a structure–crystallization behavior framework.

5.2. Existing empirical models for nepheline crystallization prediction

As cited in the introduction, several empirical models have been widely used to predict the crystallization of nepheline in alkali aluminosilicate and aluminoborosilicate glasses based solely on bulk composition. Among these, the most commonly adopted approaches are the nepheline discriminator [13] (ND), the optical basicity [5] (OB) criterion, and the submixture model [27]. These models have proven useful in identifying broad compositional trends and have been successfully applied within their original calibration domains.

The nepheline discriminator (ND) was calculated according to:

$$ND = \frac{g_{SiO2}}{g_{SiO2} + g_{Na2O} + g_{Al2O3}} \tag{2}$$

Where g_i denotes the mass fraction of oxide *i*. Glasses with ND ≥ 0.62 are conventionally predicted to be free of nepheline crystallization.

The optical basicity (OB) was calculated as a weighted average of the optical basicities of the individual oxides:

$$OB = \frac{\sum_i x_i q_i \Lambda_i}{\sum_i x_i q_i} \tag{3}$$

Where x_i is mole fraction of oxide *i*, q_i is the number of oxygen atoms in the *i*th component oxide and Λ_i is the oxide molar basicity. The parameters were taken from the literature [7] and are listed in Table S16 of the ESI. In alkali aluminoborosilicate glasses, nepheline crystallization is typically expected to be suppressed for OB values below 0.55.

The submixture model index P was computed following the formulation proposed by Vienna et al. [27], using the optimal parameter set reported in the original model. The models groups oxides into three pseudo-components A, B and C, defined as:

$$\begin{aligned} A &= g_{Na2O} + Ug_{MgO} + Yg_{Li2O} + Zg_{K2O} \\ B &= g_{Al2O3} + Wg_{Fe2O3} \\ C &= g_{SiO2} + Tg_{P2O5} + Xg_{B2O3} \end{aligned} \tag{4}$$

Where g_i are the mass fractions and the coefficients U, V, W, X, Y, Z, T are fixed model parameters. The index P is then computed as:

$$P = -\frac{bC + 2bB - \sqrt{3}C}{2(A+B+C)} - \frac{c(2B+C)^2}{4(A+B+C)^2} - a \tag{5}$$

With parameters a, b, and c taken from the optimal submixture model formulation. According to the model, glass with P < 0 are predicted to crystallize nepheline.

Fig. 2 compares the performance of these three composition-based predictors for the present dataset. The descriptors are plotted against the experimentally observed crystallization outcome (red points= Nepheline crystallizes, blue ones = does not).

As shown in Fig. 2a, the nepheline discriminator does not exhibit a clear correlation with the crystallization behavior of the investigated glasses. Red and blue points are broadly intermixed over the entire ND range, mostly on the left side of the conventional threshold value (ND = 0.62). In particular, numerous glasses predicted to be prone to nepheline crystallization according to ND remain amorphous, while others with comparable ND values do crystallize. This absence of a discernible trend indicates that, for the present multicomponent dataset, the nepheline discriminator is not suitable to discriminate crystallization propensity. A similar situation is observed for the submixture model index P, reported in Fig. 2b Despite the increased complexity of the descriptor and the grouping of oxides into pseudo-components, the values of P show a substantial overlap between crystallizing and non-crystallizing glasses. Both red and blue points are distributed across positive and negative P values, including around the nominal threshold (P = 0). As a result, the submixture model does not provide a unique separation between the two classes for the glasses investigated in this work.

In contrast, optical basicity (Fig. 2c) exhibits a clearer, although still empirical, correlation with nepheline crystallization. Most glasses that do not crystallize nepheline are concentrated at lower OB values, while crystallizing compositions tend to occupy the higher-OB region. Although some overlap remains near the commonly reported threshold range, the separation between red and blue points is visibly improved compared to ND and P. This indicates that, among the empirical composition-based descriptors considered here, optical basicity provides the most informative discrimination for the present dataset.

Based on these observations, the nepheline discriminator and the submixture model index are not considered further in the development of the predictive framework. Optical basicity is retained as the sole empirical descriptor and combined with structure-informed descriptors derived from molecular dynamics simulations, as discussed in the following section.

5.3. Structural descriptors for nepheline crystallization

The guiding hypothesis of this work is that glass crystallization correlates with the presence of structural units or atomic clusters whose composition and geometry resemble those of the crystal phase. If the structural similarities exist, atomic rearrangement into the crystal lattice becomes energetically more favorable under appropriate conditions. Due to this reason, although several compositional descriptors have been proposed in the literature [27,62], our focus was on descriptors

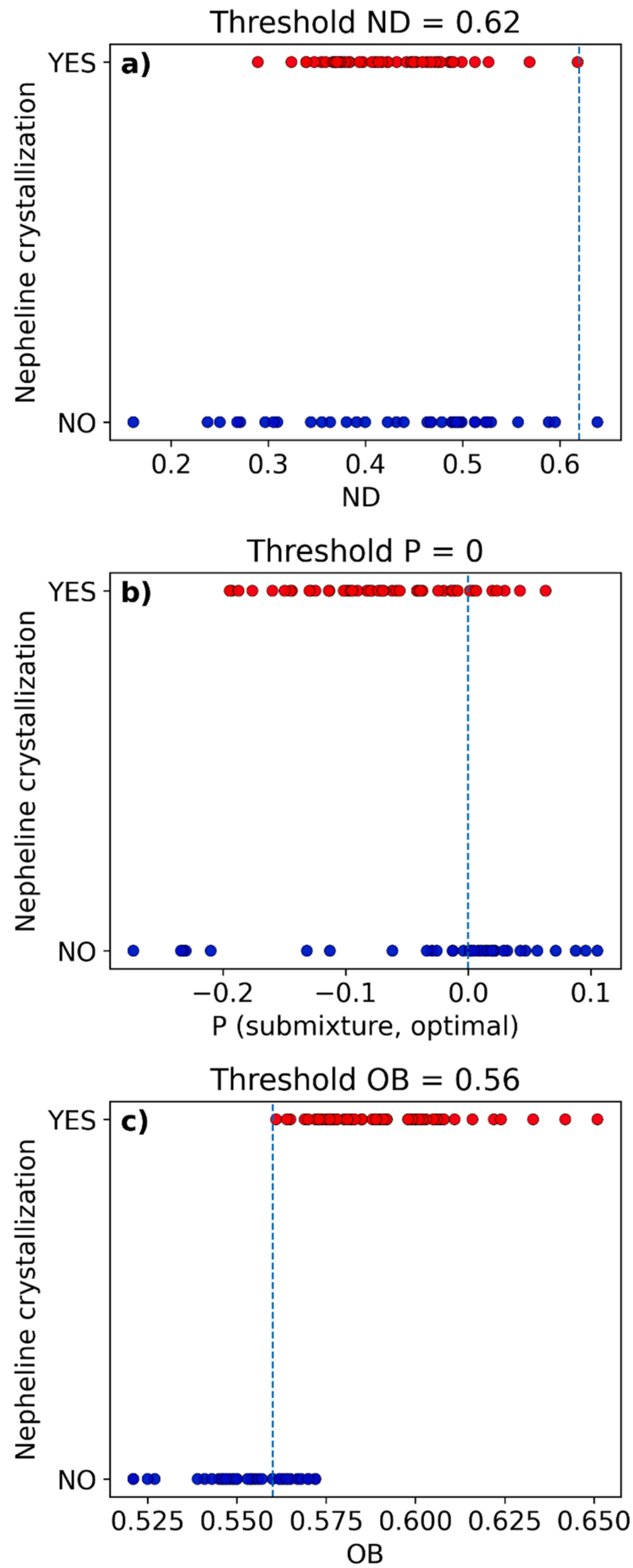

Fig. 2. Compositional descriptors vs crystallization behavior. Particularly, (a) Nepheline Discriminator; (b) Submixture Model; and (c) Optical Basicity. In each panel, red and blue dots represent glasses that crystallize or not-crystallize nepheline. The value usually identified as the crystallization threshold is reported as a vertical dashed line.

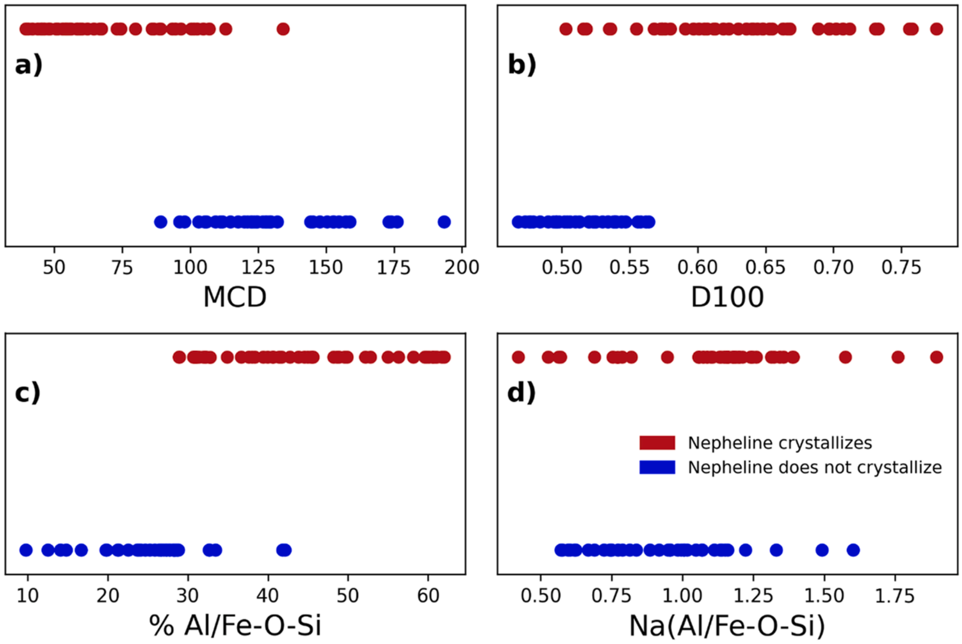

Fig. 3. Structural descriptors used in this work to predict the propensity of crystallization of nepheline in the investigated glasses: (a) MCD, (b) D_{100} descriptor, (c) % Al/Fe–O–Si bonds, (d) amount of Na/K around the Al/Fe–O–Si bonds, and (e) the OB. The red dots represent glasses that crystallize nepheline (or its polymorphs), while the blue dots represent glasses that do not crystallize.

derived directly from the simulated glass structures.

Nepheline crystal consists of Al–O–Si bonds coordinated by Na^+, with partial substitution of Al^{3+} by Fe^{3+} allowed up to a certain threshold [63](see Section S7 of the Supporting Information), while Na^+ can be completely substituted by K^+ [64]. Based on this, the MCD (Fig. 3a) and D_{100} (Fig. 3b) descriptors for all the investigated glasses were calculated using the cluster code. Then we examined the percentage of Al/Fe–O–Si linkages in the glass structure (Fig. 3c) and quantified the number of Na/K atoms in the local environment, determined using the first minimum of the Na/K–BO partial distribution function as the cutoff distance (Fig. 3d). The data reported in Fig. 3 are tabulated in **Table S16** of the ESI.

From Fig. 3, it is evident that no single descriptor can fully distinguish between glasses that crystallize (red dots) and those that do not (blue dots). With the exception of Na/K(Al–O–Si) (Fig. 3d), which fails entirely, all descriptors provide at least partial separation of the two groups, albeit with some overlap. In general, glasses with low fraction of Al/Fe–O–Si bonds (Fig. 3c), high MCD (Fig. 3a) and low fraction of D_{100} (Fig. 3b) are less likely to precipitate nepheline.[1] These observations support the hypothesis that a glass environment resembling the crystalline phase favors crystallization.

However, one-dimensional classification models based solely on a single MD-derived descriptor fail to reliably predict crystallization, as demonstrated by the overlapping regions of glass compositions. This limitation likely stems from the imperfect reproduction of experimental glass structures by classical MD simulations. Likewise, although the OB descriptor offers clearer separation between crystallizing and non-crystallizing glasses, an overlapping region persists where the model cannot definitively classify glasses by their crystallization tendency. Therefore, a correlation analysis followed by a Principal Component Analysis (PCA) was performed between the compositional, i.e., OB, and structural descriptors, i.e., MCD, %Al/Fe–O–Si, #Na/K(Al/Fe–O–Si), D_{100}, and the structural attributes, i.e., Si–O–T and Al–O–T bonds, where T = B, Si, P, coordination number of Na^+, oxygen speciation (bridging oxygens – BOs, non-bridging oxygens - NBOs and TBOs). The aim was to understand the correlations between these descriptors and structural attributes, unearth the hidden patterns, and identify potential redundancies.

Among all of the structural features and descriptors, MCD, OB, %Al/Fe–O–Si, #Na/K(Al/Fe–O–Si), and D_{100} emerged as the most important parameters for predicting crystallization. Their Pearson correlation matrix is reported in Fig. 4(a). Several strong correlations are immediately apparent, such as the positive correlation between OB and %Al/Fe–O–Si (r = 0.84), and between D_{100} and %Al/Fe–O–Si (r = 0.83), suggesting that these descriptors may encode overlapping information. In contrast, the MCD descriptor is negatively correlated with all the others, especially with D_{100} (r = –0.89), highlighting its distinct nature as a global cluster-based descriptor compared to local coordination or compositional features.

To explore whether a reduced set of variables can capture most of the structural variance among samples, we applied PCA to the standardized dataset (Fig. 4b). The biplot shows the distribution of samples in the PC1–PC2 space along with the loading vectors of the original descriptors. Crystallizing (red) and non-crystallizing (blue) glasses show some separation along PC1, with most of the non-crystallizing glasses occupying the positive side of PC1. This suggests that the first principal component effectively captures structural features relevant for distinguishing crystallization tendency. The loading plots for PC1 (Fig. 4c) and PC2 (Fig. 4d) reveal that PC1 is most strongly influenced by MCD (positive weight), D_{100} and OB (negative weights), suggesting that these variables are crucial in defining the main structural contrast among the samples. In contrast, PC2 is mainly influenced by the #Na/K(Al/Fe–O–Si) descriptor, though this component does not provide a clear separation of the classes. Overall, the PCA confirms that MCD, OB, and D_{100} are among the most informative descriptors and motivates their use in combination to enhance classification. Notably, MCD appears to encode information orthogonal to other descriptors, which is beneficial when constructing multi-dimensional models.

[1] The primary crystalline phase in glass SP-25 is $AlPO_4$, with nepheline as secondary **(Table 1)**. Accordingly, we classify SP-25 as a non-crystallizing glass. MCD calculations for SP-25, using nepheline and $AlPO_4$ crystals, yield 129.50 and 102.00, respectively, indicating that the local oxygen environment in the glass more closely resembles $AlPO_4$, confirming it as the first precipitating phase.

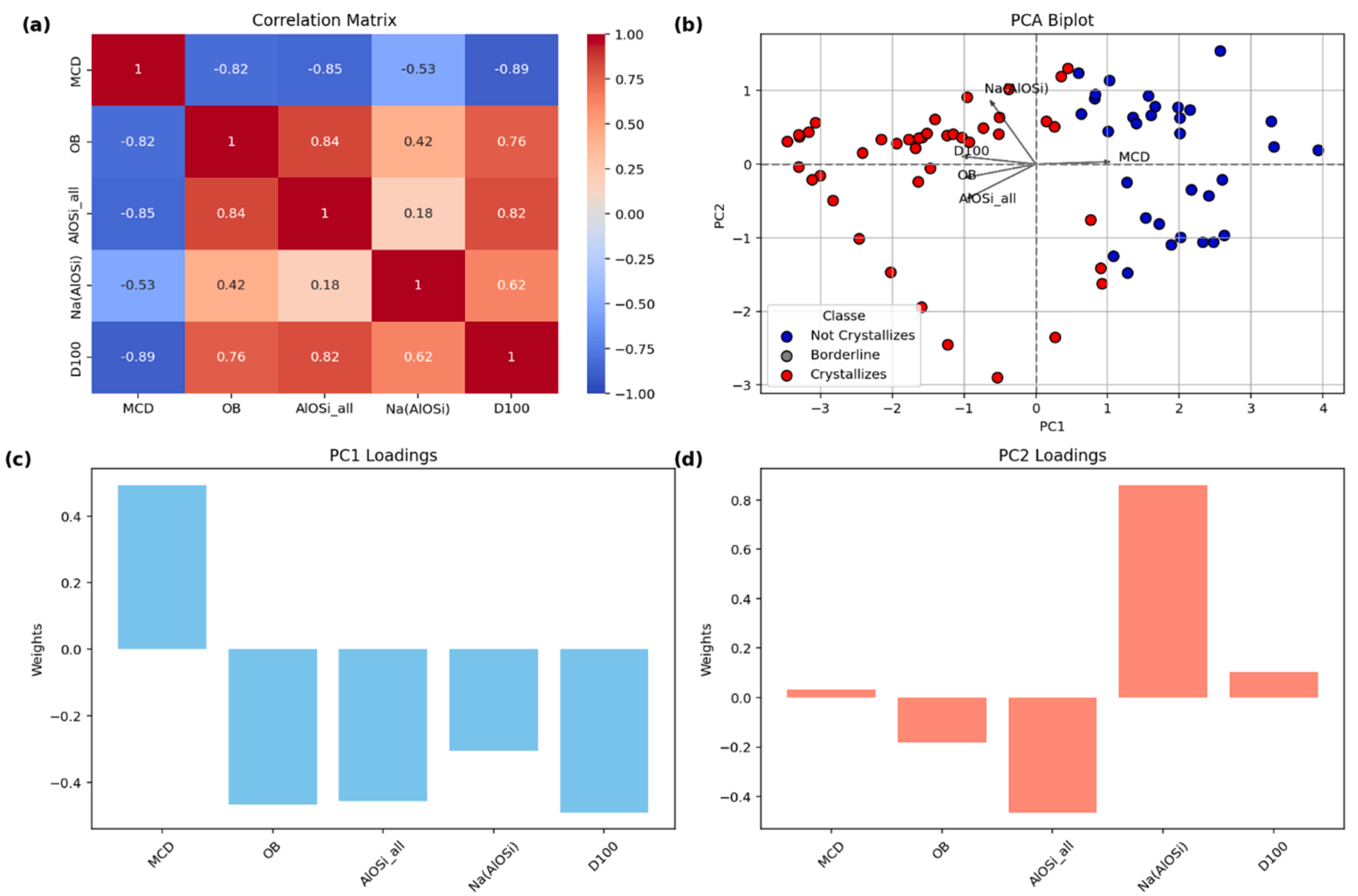

Fig. 4. Statistical analysis of structural descriptors for predicting nepheline crystallization. **(a)** Pearson correlation matrix of five structural descriptors: Mean Cluster Displacement (MCD), Optical Basicity (OB), percentage of Al/Fe–O–Si linkages, number of Na/K atoms around Al/Fe–O–Si environments, and the D_{100} descriptor, **(b)** PCA biplot showing sample distribution along the first two principal components (PC1 and PC2), with original descriptor loadings overlaid as arrows. Samples are colored by class: crystallizing (red), not crystallizing (blue), and borderline (grey), **(c)** PC1 loadings illustrate the relative contribution of each descriptor to the first principal component, **(d)** PC2 loadings show the contribution of each descriptor to the second principal component. The analysis highlights MCD, OB, and D_{100} are the most discriminative descriptors and suggests that combining multiple descriptors may improve class separation.

To enhance separation power, we explored combining the descriptors into 2D models. Excluding the Na/K(Al–O–Si), we tested all combinations of the MCD, D_{100}, %Al/Fe–O–Si, and OB. The results are reported in Fig. 5. Combining descriptors clearly enhances the separation between crystallizing and non-crystallizing domains, although some misclassifications remain. Among all the combinations, the MCD vs OB (Fig. 5a) provides the most accurate separation, with only single misclassified point (BL_Li), whereas other combinations exhibit overlapping regions. The BL_Li glass crystallizes 2.8 vol.% of Si-rich nepheline [12]. This misclassification likely arises from the discrepancy between the reference crystal used in the CLUSTER analysis and the actual phase precipitating from this glass, as well as its inherently low crystallization tendency.

These results highlight that the interplay between compositional and structural descriptors is crucial for delineating crystallization domains with the observed level of accuracy. Improving the fidelity of structural description – through structural refinement procedures or the adoption of more accurate interatomic potentials – is expected to improve the classification capability of the MCD and related metrics, potentially reducing or even eliminating the need for compositional descriptors.

To further assess potential improvements in separation of crystallization domains, we also tested combinations of more than two descriptors. For example, Fig. 6 presents a 3D plot combining MCD, OB, and %Al/Fe–O–Si. Similarly, tests with other combinations were conducted; however, no improvement in the model predictability was observed.

We further attempted to use the proposed descriptors to distinguish between glasses that crystallize low-carnegieite (orthorhombic $NaAlSiO_4$) and those that crystallize nepheline (hexagonal $NaAlSiO_4$) as the primary or sole crystalline phase. Using the combination of MCD and OB (Fig. 7), we observed that carnegieite-forming glasses exhibit very low MCD values (<60) and generally high OB (>0.575). Notably, glasses yielding only carnegieite show the highest OB and fall within the region associated with the greatest crystallization tendency. This indicates that carnegieite precipitates only when the glass environment is highly alkaline and structurally well aligned with the $NaAlSiO_4$ crystal structure, whereas nepheline preferentially forms under less alkaline conditions—for instance, in B_2O_3- or P_2O_5-containing glasses [25,31,58] with comparatively lower degree of structural similarity to crystalline $NaAlSiO_4$.

In our model, glasses crystallizing carnegieite generally separate from those forming nepheline, though some overlap remains. The limited number of carnegieite-forming compositions prevents us from determining whether a complete separation is achievable, but the present results motivate further investigation. Moreover, recalculating MCD using the carnegieite crystal does not yield significantly different values, since the cluster compositions are very similar to nepheline.

5.4. Machine learning classification models

The combination of MCD and OB data gives the optimal visual differentiation between the crystallization domains. Fig. 7 shows that the

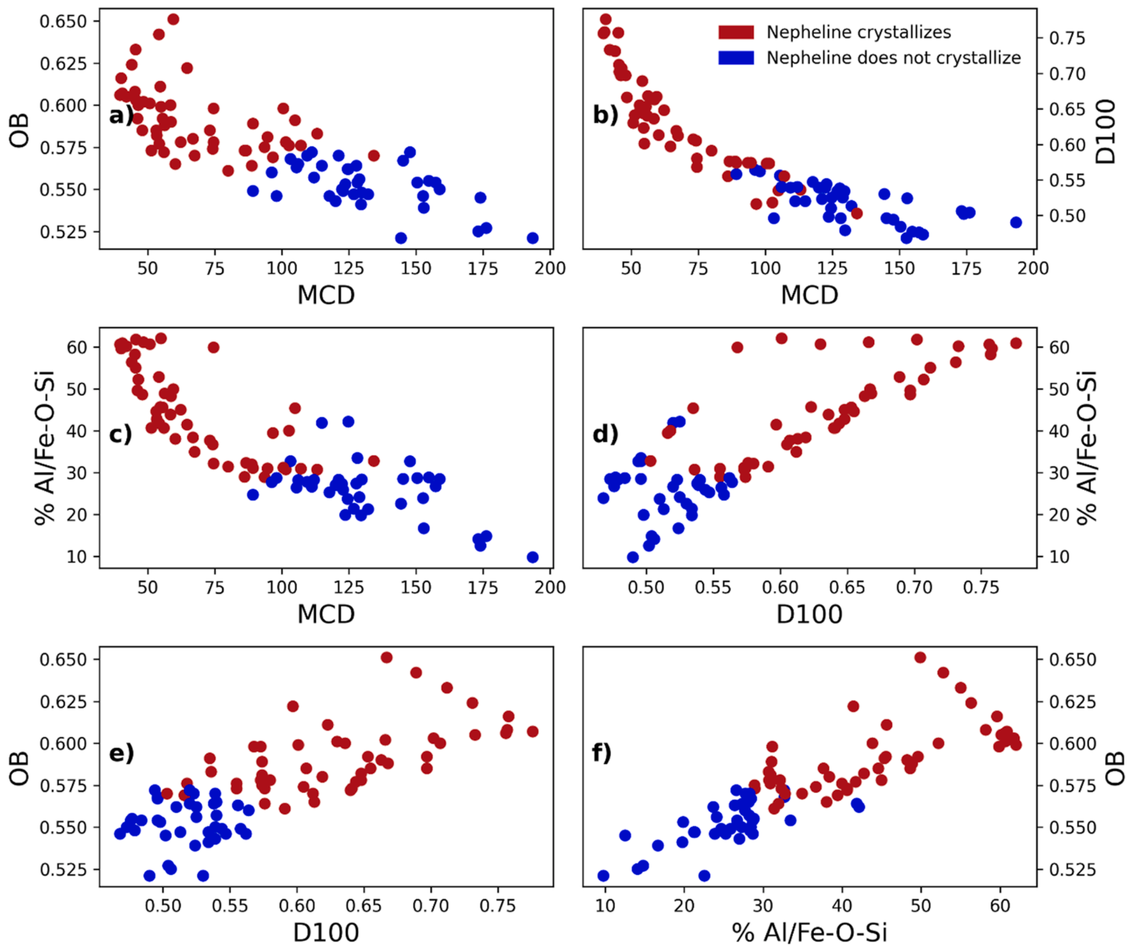

Fig. 5. A combination of the structural descriptors tested in this work. The red dots represent glasses that crystallize nepheline (or carnegieite) and the blue dots represent glasses that do not crystallize. Panel (a) MCD vs OB, (b), MCD vs D_{100}, (c) MCD vs %Al/Fe–O–Si, (d) D_{100} vs %Al/Fe–O–Si, (e) D_{100} vs OB, and (f) %Al/Fe–O–Si vs OB.

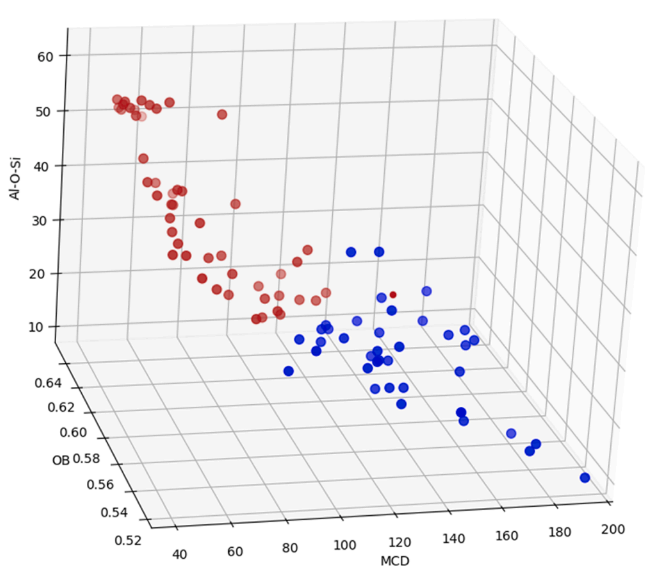

Fig. 6. 3D representation of the MCD vs OB vs %Al/Fe–O–Si data. Red dots represent glasses that crystallize nepheline (or carnegieite) and blue dots represent glasses that do not crystallize.

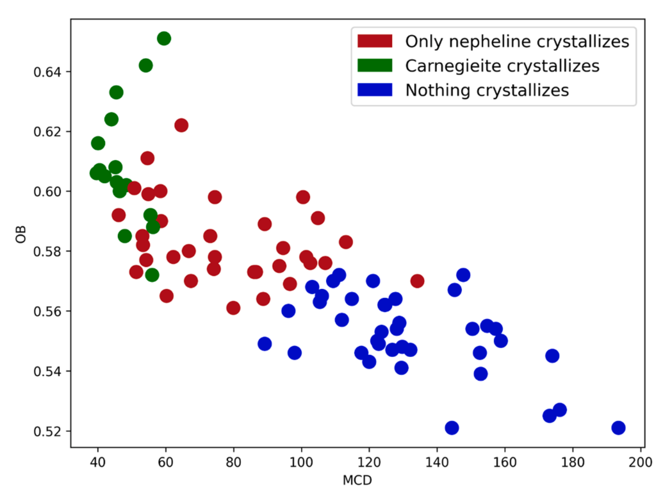

Fig. 7. MCD vs OB plot. Red dots represent glasses that only precipitate nepheline, green dots represent glasses precipitating also or only carnegieite, while blue dots represent glasses that do not crystallize.

BL_Li glass, which crystallizes only a small amount of Si-rich nepheline, lies within the non-crystallization region of the descriptor space and close to the decision boundary. This marginal position highlights the

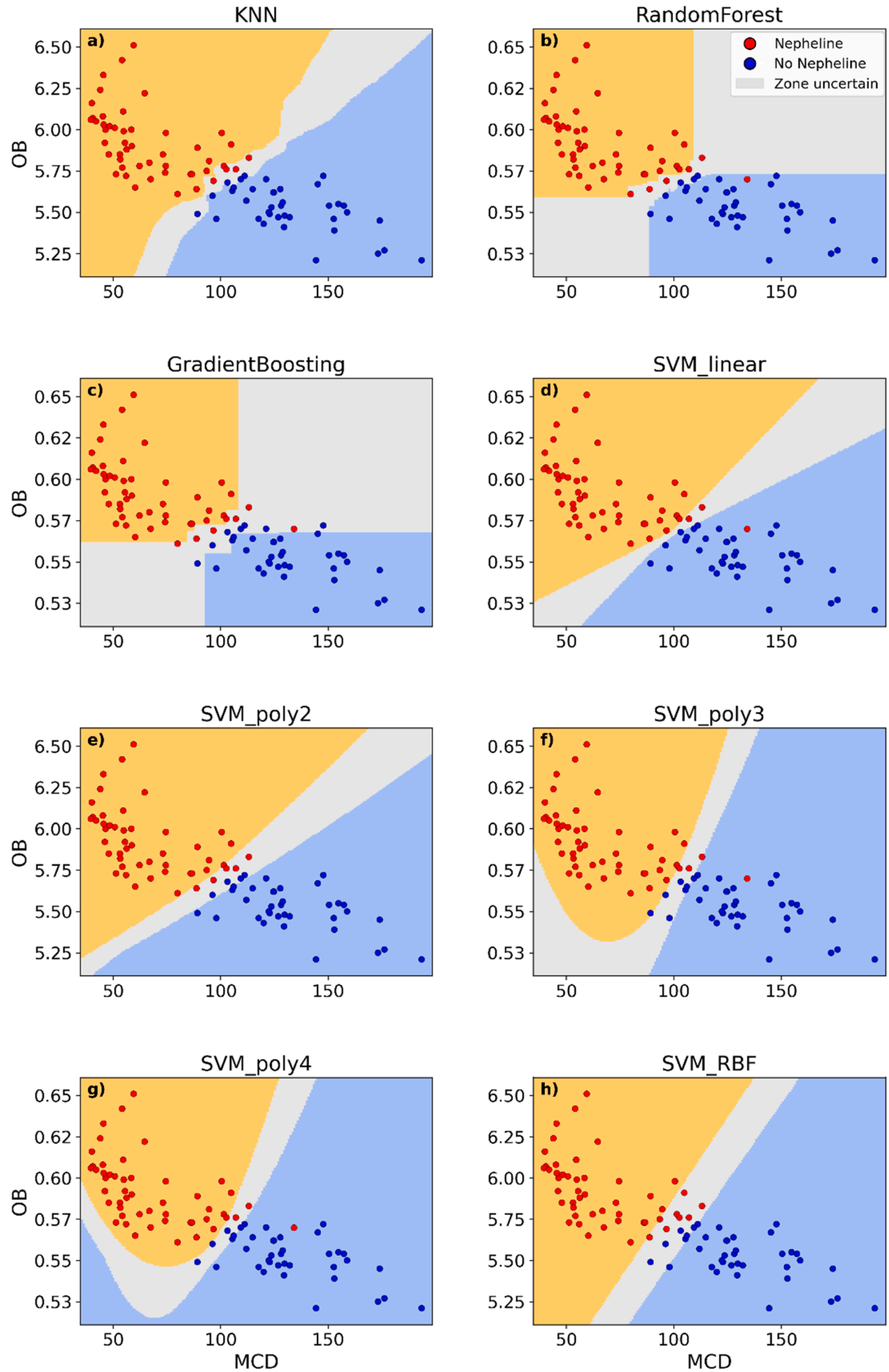

Fig. 8. Classification of the (a) KNN; (b) RF; (c) GB; (d) linear SVM; polynomial SVM (e) 2nd degree, (f) 3rd degree, (g) 4th degree; (h) RBF SVM. Red dots indicate glasses that crystallize nepheline and blue dots indicate glasses that do not crystallize nepheline. Orange and blue areas represent the predicted portion of the MCD vs OB space where nepheline crystallizes or does not crystallize, respectively. Grey regions indicate areas of model uncertainty arising from disagreement across cross-validation folds and/or from extrapolation into sparsely sampled regions of the descriptor space; they do not represent statistical confidence intervals.

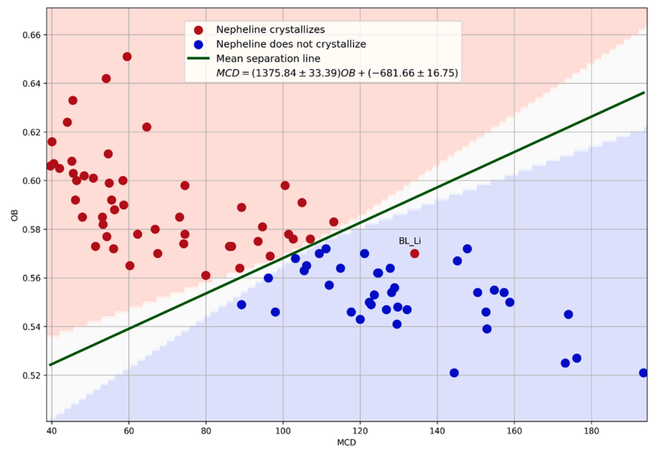

Fig. 9. SVM linear model using MCD and OB to predict nepheline crystallization from glass matrices. Red dots represent glasses that crystallize nepheline or carnegieite, blue dots represent glasses that do not crystallize nepheline. Red areas indicate the predicted portion of the MCD vs OB space where nepheline crystallizes or does not crystallize, respectively, while the grey area is the uncertainty region given by the repeated 5-fold CV.

sensitivity of lithium-rich compositions and underscores the limits of the present descriptor set in fully capturing their crystallization behavior. Fig. 8 summarizes the performance of tested MLCs, with accuracy reported as an average over five iterations of 5-cross validation procedure used and reported in Table S17, as well as precision, recall, and F1 score metrics.

All models achieved $>$90% accuracy in predicting nepheline crystallization within our database, while the linear SVM performed best (94.1% accuracy). Each classifier predicts a crystallization region at high OB and low MCD and a no-crystallization domain at low OB and high MCD, separated by an uncertainty region of varying extent. These grey regions do not represent statistical confidence intervals. Instead, they highlight regions of reduced prediction reliability arising from two complementary effects. First, they identify areas where different cross-validation realizations lead to different class predictions, indicating sensitivity of the decision boundary to data resampling. Second, grey regions also appear in portions of the (MCD, optical basicity) space that are sparsely sampled or entirely unsampled by the available glass compositions. In these cases, model predictions correspond to extrapolation rather than interpolation and are therefore intentionally flagged as uncertain. This representation is meant to prevent overinterpretation and to explicitly indicate where additional data would be required to improve predictive robustness.

Among the tested classifiers, the linear SVM provides the most compact uncertainty region and consistently high classification performance, while yielding a simple and directly interpretable analytical separation between crystallization and non-crystallization domains. In contrast, more flexible models such as polynomial or RBF SVMs, k-nearest neighbors, gradient boosting, or random forests, rely on higher dimensional parameterizations and, in some cases, on the explicit retention of support vectors or training samples, which makes physical interpretation of the resulting decision boundaries less transparent. For these reasons, we selected the linear SVM as the preferred model.

The final separation line was obtained by averaging the slope and intercept values extracted from all realizations of the repeated 5-fold CV procedure, with the associated standard deviations (Fig. 9) reflecting the variability of the decision boundary under data resampling rather than statistical fitting errors. The resulting boundary can be represented as:

$$MCD = (1375.84 \pm 33.39)OB + (-681.66 \pm 16.75)$$

Although the numerical uncertainties on the slope and intercept appear sizable when considered in isolation, their impact on the position of the decision boundary in descriptor space is limited, and the classification of most glasses remains unchanged across cross-validation realizations. Glasses located above this line are therefore predicted to crystallize nepheline, whereas those below are not, with uncertainty confined to a narrow region around the boundary.

6. Conclusions

In this study, we developed a predictive framework that integrates systematic experimental datasets, MD simulations, and machine learning to forecast crystallization in multicomponent alkali aluminoborosilicate glasses designed in the crystallization field of nepheline ($NaAlSiO_4$). Using nepheline ($NaAlSiO_4$)-crystalline phase as a model system, we demonstrated that medium-range structural motifs embedded in glass correlate with crystallization behavior. A new structural descriptor, the Mean Cumulative Displacement (MCD), was introduced to quantify the structural similarity between glass and nepheline crystal. When combined with optical basicity, MCD enabled robust separation of crystallizing and non-crystallizing glasses.

Validation of MD models against multinuclear MAS NMR spectra confirmed the accuracy of the simulated structures. Machine learning classifiers trained on the MCD and OB descriptors achieved predictive accuracies above 94%, with the linear support vector machine providing both the highest performance and interpretable decision boundaries that link composition, structure to crystallization propensity.

The methodology presented here establishes a structure-based route to predict crystallization in multicomponent glasses, as demonstrated for nepheline in alkali alumino-boro-phospho-silicate systems. Extending this framework to other crystalline phases and glass families will require additional validation and is the subject of ongoing and future work. More broadly, it will possibly offer a paradigm shift in glass science, enabling the accelerated design of stable glasses and functional glass-ceramics for applications ranging from nuclear waste immobilization to advanced optical and structural materials.

Data Availability

The dataset of compositions and descriptors, the CLUSTER code for MCD and D100 calculation, and the script used to generate the tested classifiers are available at …

CRediT authorship contribution statement

Marco Bertani: Writing – original draft, Supervision, Methodology, Investigation. **Matilde Benassi:** Writing – review & editing, Investigation, Data curation. **Lorenzo Gottardi:** Writing – review & editing, Investigation. **Gianluca Malavasi:** Writing – review & editing, Investigation. **Ashutosh Goel:** Writing – original draft, Methodology, Funding acquisition. **Alfonso Pedone:** Writing – original draft, Supervision, Methodology, Funding acquisition, Conceptualization.

Declaration of competing interest

The authors declare that they have no known competing financial interests or personal relationships that could have appeared to influence the work reported in this paper.

Acknowledgments

This material is based upon work supported by (1) PNRR MUR project CS_00000033_ECOSISTER; (2) NVIDIA Academic Hardware Grant Program; (3) US National Science Foundation under Grant No 2034871; (4) US Department of Energy (DOE), Hanford Field Office, through contract number 89304022CEM000015.

Supplementary materials

Supplementary material associated with this article can be found, in the online version, at doi:10.1016/j.actamat.2026.122216.

References

[1] V.M. Fokin, E.D. Zanotto, N.S. Yuritsyn, J.W.P. Schmelzer, Homogeneous crystal nucleation in silicate glasses: a 40 years perspective, J. Non-Cryst. Solids 352 (2006) 2681–2714, https://doi.org/10.1016/j.jnoncrysol.2006.02.074.

[2] J.C. Mauro, E.D. Zanotto, Two centuries of glass research: historical trends, current status, and grand challenges for the future, Int. J. Appl. Glass. Sci. 5 (2014) 313–327, https://doi.org/10.1111/ijag.12087.

[3] E.D. Zanotto, J.E. Tsuchida, J.F. Schneider, H. Eckert, Thirty-year quest for structure–nucleation relationships in oxide glasses, Int. Mater. Rev. 60 (2015) 376–391, https://doi.org/10.1080/09506608.2015.1114706.

[4] K.F. Kelton, A.L. Greer, Chapter 8 - crystallization in glasses, in: K.F. Kelton, A. L. Greer (Eds.), Pergamon Materials Series, Pergamon, 2010, pp. 279–329, https://doi.org/10.1016/S1470-1804(09)01508-9.

[5] J.S. McCloy, M.J. Schweiger, C.P. Rodriguez, J.D. Vienna, Nepheline crystallization in nuclear waste glasses: progress toward acceptance of high-alumina formulations, Int. J. Appl. Glass. Sci. 2 (2011) 201–214, https://doi.org/10.1111/j.2041-1294.2011.00055.x.

[6] A. Goel, J.S. McCloy, R. Pokorny, A.A. Kruger, Challenges with vitrification of Hanford high-level waste (HLW) to borosilicate glass – an overview, J. Non-Cryst. Solids X 4 (2019) 100033, https://doi.org/10.1016/j.nocx.2019.100033.

[7] J.S. McCloy, M.J. Schweiger, C.P. Rodriguez, J.D. Vienna, Nepheline crystallization in nuclear waste glasses: progress toward acceptance of high-alumina formulations, Int. J. Appl. Glass. Sci. 2 (2011) 201–214, https://doi.org/10.1111/j.2041-1294.2011.00055.x.

[8] I. Sargin, C.E. Lonergan, J.D. Vienna, J.S. McCloy, S.P. Beckman, A data-driven approach for predicting nepheline crystallization in high-level waste glasses, J. Am. Ceram. Soc. 103 (2020) 4913–4924, https://doi.org/10.1111/jace.17122.

[9] J.D. Vienna, J.O. Kroll, P.R. Hrma, J.B. Lang, J.V. Crum, Submixture model to predict nepheline precipitation in waste glasses, Int. J. Appl. Glass. Sci. 8 (2017) 143–157, https://doi.org/10.1111/ijag.12207.

[10] A. Goel, J.S. McCloy, R. Pokorny, A.A. Kruger, Challenges with vitrification of Hanford high-level waste (HLW) to borosilicate glass – an overview, J. Non-Cryst. Solids X 4 (2019) 100033, https://doi.org/10.1016/j.nocx.2019.100033.

[11] D.A. Duke, J.F. MacDowell, B.R. Karstetter, Crystallization and chemical strengthening of nepheline glass-ceramics, J. Am. Ceram. Soc. 50 (1967) 67–74, https://doi.org/10.1111/j.1151-2916.1967.tb15041.x.

[12] A. Deshkar, B. Parruzot, R.E. Youngman, O. Gulbiten, J.D. Vienna, A. Goel, Compositional dependence of crystallization and chemical durability in alkali aluminoborosilicate glasses, J. Non-Cryst. Solids 590 (2022) 121694, https://doi.org/10.1016/j.jnoncrysol.2022.121694.

[13] K.M. Fox, T.B. Edwards, D.K. Peeler, Control of nepheline crystallization in nuclear waste glass, Int. J. Appl. Ceram. Technol. 5 (2008) 666–673, https://doi.org/10.1111/j.1744-7402.2008.02250.x.

[14] X. Lu, I. Sargin, J.D. Vienna, Predicting nepheline precipitation in waste glasses using ternary submixture model and machine learning, J. Am. Ceram. Soc. 104 (2021) 5636–5647, https://doi.org/10.1111/jace.17983.

[15] J.D. Vienna, J.O. Kroll, P.R. Hrma, J.B. Lang, J.V. Crum, Submixture model to predict nepheline precipitation in waste glasses, Int. J. Appl. Glass. Sci. 8 (2017) 143–157, https://doi.org/10.1111/ijag.12207.

[16] X. Lu, I. Sargin, J.D. Vienna, Predicting nepheline precipitation in waste glasses using ternary submixture model and machine learning, J. Am. Ceram. Soc. 104 (2021) 5636–5647, https://doi.org/10.1111/jace.17983.

[17] Y. Zhang, M. Bertani, A. Pedone, R.E. Youngman, G. Tricot, A. Kumar, A. Goel, Decoding crystallization behavior of aluminoborosilicate glasses: from structural descriptors to quantitative structure – property relationship (QSPR) based predictive models, Acta Mater. 268 (2024) 119784, https://doi.org/10.1016/j.actamat.2024.119784.

[18] F. Lodesani, M.C. Menziani, K. Maeda, Y. Takato, S. Urata, A. Pedone, Disclosing crystal nucleation mechanism in lithium disilicate glass through molecular dynamics simulations and free-energy calculations, Sci. Rep. 10 (2020) 1–14, https://doi.org/10.1038/s41598-020-74764-9.

[19] G. Lusvardi, G. Malavasi, L. Menabue, M.C. Menziani, A. Pedone, U. Segre, A computational tool for the prediction of crystalline phases obtained from controlled crystallization of glasses, J. Phys. Chem. B 109 (2005) 21586–21592, https://doi.org/10.1021/jp0546857.

[20] E.D. Zanotto, D.R. Cassar, The microscopic origin of the extreme glass-forming ability of albite and B2O3, Sci. Rep. 7 (2017) 43022, https://doi.org/10.1038/srep43022.

[21] Y. Zhang, M. Bertani, A. Pedone, R.E. Youngman, G. Tricot, A. Kumar, A. Goel, Decoding crystallization behavior of aluminoborosilicate glasses: from structural descriptors to quantitative structure – property relationship (QSPR) based predictive models, Acta Mater. 268 (2024) 119784, https://doi.org/10.1016/j.actamat.2024.119784.

[22] V.R. Mastelaro, E.D. Zanotto, N. Lequeux, R. Cortès, Relationship between short-range order and ease of nucleation in Na2Ca2Si3O9, CaSiO3 and PbSiO3 glasses, J. Non-Cryst. Solids 262 (2000) 191–199, https://doi.org/10.1016/S0022-3093(99)00685-7.

[23] G. Lusvardi, G. Malavasi, L. Menabue, M.C. Menziani, A. Pedone, U. Segre, A computational tool for the prediction of crystalline phases obtained from controlled crystallization of glasses, J. Phys. Chem. B 109 (2005) 21586–21592, https://doi.org/10.1021/jp0546857.

[24] A. Deshkar, J. Marcial, S.A. Southern, L. Kobera, D.L. Bryce, J.S. McCloy, A. Goel, Understanding the structural origin of crystalline phase transformations in nepheline (NaAlSiO4)-based glass-ceramics, J. Am. Ceram. Soc. 100 (2017) 2859–2878, https://doi.org/10.1111/jace.14845.

[25] A. Deshkar, O. Gulbiten, R.E. Youngman, J.C. Mauro, A. Goel, Why does B2O3 suppress nepheline (NaAlSiO4) crystallization in sodium aluminosilicate glasses? Phys. Chem. Chem. Phys. 22 (2020) 8679–8698, https://doi.org/10.1039/D0CP00172D.

[26] P. Lu, S. Kapoor, L. Kobera, J. Brus, A. Goel, Structural dependence of crystallization in phosphorus-containing sodium aluminoborosilicate glasses, J. Am. Ceram. Soc. 105 (2022) 2556–2574, https://doi.org/10.1111/jace.18256.

[27] J.D. Vienna, J.O. Kroll, P.R. Hrma, J.B. Lang, J.V. Crum, Submixture model to predict nepheline precipitation in waste glasses, Int. J. Appl. Glass. Sci. 8 (2017) 143–157, https://doi.org/10.1111/ijag.12207.

[28] Y. Zhang, N. Balasubramanya, N. Stone-Weiss, S. Kamali, R.E. Youngman, P. Florian, A. Goel, Insights into the iron- and phosphorus-induced structural rearrangements in sodium aluminoborosilicate glasses and their impact on melt rheology and crystallization behavior, J. Phys. Chem. C 126 (2022) 21771–21792, https://doi.org/10.1021/acs.jpcc.2c06717.

[29] Y. Zhang, M. Bertani, A. Pedone, R.E. Youngman, G. Tricot, A. Kumar, A. Goel, Decoding crystallization behavior of aluminoborosilicate glasses: from structural descriptors to quantitative structure – property relationship (QSPR) based predictive models, Acta Mater. 268 (2024) 119784, https://doi.org/10.1016/j.actamat.2024.119784.

[30] D.L. Hamilton, W.S. MacKenzie, Phase-equilibrium studies in the system NaAlSiO4 (nepheline)–KAlSiO4 (kalsilite)–SiO2-H2O, Miner. Mag. J. Miner. Soc. 34 (1965) 214–231, https://doi.org/10.1180/minmag.1965.034.268.17.

[31] P. Lu, Y. Zan, J. Ren, T. Zhao, K. Xu, A. Goel, Structure and crystallization behavior of phosphorus-containing nepheline (NaAlSiO4) based sodium aluminosilicate glasses, J. Non-Cryst. Solids 560 (2021) 120719, https://doi.org/10.1016/j.jnoncrysol.2021.120719.

[32] B.G. Dick, A.W. Overhauser, Theory of the dielectric constants of alkali halide crystals, Phys. Rev. 112 (1958) 90–103, https://doi.org/10.1103/PhysRev.112.90.

[33] A. Tilocca, N.H. de Leeuw, A.N. Cormack, Shell-model molecular dynamics calculations of modified silicate glasses, Phys. Rev. B 73 (2006) 104209, https://doi.org/10.1103/PhysRevB.73.104209.

[34] A. Tilocca, A.N. Cormack, N.H. de Leeuw, The structure of bioactive silicate glasses: new insight from molecular dynamics simulations, Chem. Mater. 19 (2007) 95–103, https://doi.org/10.1021/cm061631g.

[35] E. Gambuzzi, A. Pedone, M.C. Menziani, F. Angeli, D. Caurant, T. Charpentier, Probing silicon and aluminium chemical environments in silicate and aluminosilicate glasses by solid state NMR spectroscopy and accurate first-principles calculations, Geochim. Cosmochim. Acta 125 (2014) 170–185, https://doi.org/10.1016/j.gca.2013.10.025.

[36] X. Xu, M. Bertani, R. Saini, S. Kamali, D.R. Neuville, R.E. Youngman, A. Pedone, A. Goel, Iron-induced structural rearrangements and their impact on sulfur solubility in borosilicate-based nuclear waste glasses, J. Phys. Chem. C 128 (2024) 11870–11887, https://doi.org/10.1021/acs.jpcc.4c02085.

[37] B. Stevensson, Y. Yu, M. Edén, Structure–composition trends in multicomponent borosilicate-based glasses deduced from molecular dynamics simulations with improved B–O and P–O force fields, Phys. Chem. Chem. Phys. 20 (2018) 8192–8209, https://doi.org/10.1039/C7CP08593A.

[38] N. Stone-Weiss, H. Bradtmüller, M. Fortino, M. Bertani, R.E. Youngman, A. Pedone, H. Eckert, A. Goel, Combined experimental and computational approach toward the structural design of borosilicate-based bioactive glasses, J. Phys. Chem. C 124 (2020) 17655–17674, https://doi.org/10.1021/acs.jpcc.0c04470.

[39] W. Smith, T.R. Forester, DL_POLY_2.0: a general-purpose parallel molecular dynamics simulation package, J. Mol. Graph. 14 (1996) 136–141.

[40] H.J.C. Berendsen, J.R. Grigera, T.P. Straatsma, The missing term in effective pair potentials, J. Phys. Chem. 91 (1987) 6269–6271, https://doi.org/10.1021/j100308a038.

[41] A.R. Leach, Molecular Modelling: Principles and Applications, Pearson Education, 2001.

[42] T. Charpentier, M.C. Menziani, A. Pedone, Computational simulations of solid state NMR spectra: a new era in structure determination of oxide glasses, RSC. Adv. 3 (2013) 10550–10578, https://doi.org/10.1039/c3ra40627j.

[43] A. Pedone, Recent advances in solid-State NMR computational spectroscopy: the case of alumino-silicate glasses, Int. J. Quantum. Chem. 116 (2016) 1520–1531, https://doi.org/10.1002/qua.25134.

[44] T. Charpentier, The PAW/GIPAW approach for computing NMR parameters: a new dimension added to NMR study of solids, Solid. State Nucl. Magn. Reson. 40 (2011) 1–20, https://doi.org/10.1016/j.ssnmr.2011.04.006.

[45] D. Presti, A. Pedone, D. Licari, V. Barone, A modular implementation for the simulation of 1D and 2D solid-State NMR spectra of quadrupolar nuclei in the virtual multifrequency spectrometer-draw graphical interface, J. Chem. Theory. Comput. 13 (2017) 2215–2229, https://doi.org/10.1021/acs.jctc.7b00154.

[46] E. Berardo, A. Pedone, P. Ugliengo, M. Corno, DFT modeling of 45S5 and 77S soda-lime phospho-silicate glass surfaces: clues on different bioactivity mechanism, Langmuir 29 (2013) 5749–5759, https://doi.org/10.1021/la304795w.

[47] M. Fortino, A. Berselli, N. Stone-Weiss, L. Deng, A. Goel, J. Du, A. Pedone, Assessment of interatomic parameters for the reproduction of borosilicate glass structures via DFT-GIPAW calculations, J. Am. Ceram. Soc. 102 (2019) 7225–7243, https://doi.org/10.1111/jace.16655.

[48] E. Gambuzzi, T. Charpentier, M.C. Menziani, A. Pedone, Computational interpretation of Na-23 MQMAS NMR spectra: a comprehensive investigation of

the Na environment in silicate glasses, Chem. Phys. Lett. 612 (2014) 56–61, https://doi.org/10.1016/j.cplett.2014.08.004.

[49] E. Gambuzzi, A. Pedone, M.C. Menziani, F. Angeli, P. Florian, T. Charpentier, Calcium environment in silicate and aluminosilicate glasses probed by Ca-43 MQMAS NMR experiments and MD-GIPAW calculations, Solid. State Nucl. Magn. Reson. 68–69 (2015) 31–36, https://doi.org/10.1016/j.ssnmr.2015.04.003.

[50] A. Pedone, T. Charpentier, M.C. Menziani, Multinuclear NMR of CaSiO3 glass: simulation from first-principles, Phys. Chem. Chem. Phys. 12 (2010) 6054–6066, https://doi.org/10.1039/b924489a.

[51] A. Pedone, T. Charpentier, M.C. Menziani, The structure of fluoride-containing bioactive glasses: new insights from first-principles calculations and solid state NMR spectroscopy, J. Mater. Chem. 22 (2012) 12599–12608, https://doi.org/10.1039/c2jm30890h.

[52] A. Pedone, E. Gambuzzi, G. Malavasi, M.C. Menziani, First-principles simulations of the Al-27 and O-17 solid-state NMR spectra of the CaAl2Si3O10 glass, Theor. Chem. Acc. 131 (2012) 1147, https://doi.org/10.1007/s00214-012-1147-5.

[53] M. Ahmadzadeh, J. Marcial, J. McCloy, Crystallization of iron-containing sodium aluminosilicate glasses in the NaAlSiO4-NaFeSiO4 join, J. Geophys. Res. Solid. Earth. 122 (2017) 2504–2524, https://doi.org/10.1002/2016JB013661.

[54] A. Pedone, Recent advances in solid-state NMR computational spectroscopy: the case of alumino-silicate glasses, Int. J. Quantum. Chem. 116 (2016) 1520–1531, https://doi.org/10.1002/qua.25134.

[55] H. Grussaute, L. Montagne, G. Palavit, J.L. Bernard, Phosphate speciation in Na2O–CaO–P2O5–SiO2 and Na2O–TiO2–P2O5–SiO2 glasses, J. Non-Cryst. Solids 263–264 (2000) 312–317, https://doi.org/10.1016/S0022-3093(99)00643-2.

[56] N. Stone-Weiss, H. Bradtmüller, M. Fortino, M. Bertani, R.E. Youngman, A. Pedone, H. Eckert, A. Goel, Combined experimental and computational approach toward the structural design of borosilicate-based bioactive glasses, J. Phys. Chem. C 124 (2020) 17655–17674, https://doi.org/10.1021/acs.jpcc.0c04470.

[57] M.J. Toplis, T. Schaller, A 31P<math><msup><mi></mi><mn>31</mn></msup><mtext>P</mtext></math>MAS NMR study of glasses in the system *x*Na2O–(1−*x*)Al2O3–2SiO2–*y*P2O5, J. Non-Cryst. Solids 224 (1998) 57–68, https://doi.org/10.1016/S0022-3093(97)00458-4.

[58] P. Lu, S. Kapoor, L. Kobera, J. Brus, A. Goel, Structural dependence of crystallization in phosphorus-containing sodium aluminoborosilicate glasses, J. Am. Ceram. Soc. 105 (2022) 2556–2574, https://doi.org/10.1111/jace.18256.

[59] A. Nizamutdinova, T. Uesbeck, T. Grammes, D.S. Brauer, L. van Wüllen, Structural role of phosphate in metaluminous sodium aluminosilicate glasses As studied by solid State NMR spectroscopy, J. Phys. Chem. B 124 (2020) 2691–2701, https://doi.org/10.1021/acs.jpcb.9b11403.

[60] M. Bertani, A. Pallini, M. Cocchi, M.C. Menziani, A. Pedone, A new self-consistent empirical potential model for multicomponent borate and borosilicate glasses, J. Am. Ceram. Soc. 105 (2022) 7254–7271, https://doi.org/10.1111/jace.18681.

[61] B. Stevensson, Y. Yu, M. Edén, Structure–composition trends in multicomponent borosilicate-based glasses deduced from molecular dynamics simulations with improved B–O and P–O force fields, Phys. Chem. Chem. Phys. 20 (2018) 8192–8209, https://doi.org/10.1039/C7CP08593A.

[62] J.S. McCloy, M.J. Schweiger, C.P. Rodriguez, J.D. Vienna, Nepheline crystallization in nuclear waste glasses: progress toward acceptance of high-alumina formulations, Int. J. Appl. Glass. Sci. 2 (2011) 201–214, https://doi.org/10.1111/j.2041-1294.2011.00055.x.

[63] M. Ahmadzadeh, J. Marcial, J. McCloy, Crystallization of iron-containing sodium aluminosilicate glasses in the NaAlSiO4-NaFeSiO4 join, J. Geophys. Res. Solid. Earth. 122 (2017) 2504–2524, https://doi.org/10.1002/2016JB013661.

[64] D.L. Hamilton, W.S. MacKenzie, Phase-equilibrium studies in the system NaAlSiO4 (nepheline)–KAlSiO4 (kalsilite)–SiO2-H2O, Miner. Mag. J. Miner. Soc. 34 (1965) 214–231, https://doi.org/10.1180/minmag.1965.034.268.17.